Nuclear Instruments and Methods in Physics Research A 695 (2012) 129–134

Contents lists available at SciVerse ScienceDirect

Nuclear Instruments and Methods in Physics Research A

journal homepage: www.elsevier.com/locate/nima

AX-PET: A novel PET concept with G-APD readout

E. Bolle[h], C. Casella[c], E. Chesi[f], R. De Leo[e], G. Dissertori[c], V. Fanti[b], J.E. Gillam[d], M. Heller[a,*], C. Joram[a], W. Lustermann[c], E. Nappi[e], J.F. Oliver[d], F. Pauss[c], M. Rafecas[d], A. Rudge[f], U. Ruotsalainen[g,i,j], D. Schinzel[c,1], T. Schneider[a], J. Séguinot[a], P. Solevi[d], S. Stapnes[h], U. Tuna[j], P. Weilhammer[f]

[a] CERN, PH Department, CH-1211 Geneva, Switzerland
[b] Università e Sezione INFN di Cagliari, Italy
[c] Institute for Particle Physics, ETH Zurich, CH-8093 Zurich, Switzerland
[d] IFIC (Universidad de Valencia/CSIC), E-46071 Valencia, Spain
[e] INFN, Sezione di Bari, I-70122 Bari, Italy
[f] Ohio State University, Columbus, Ohio 43210, USA
[g] University of Michigan, Ann Arbor, MI 48109, USA
[h] University of Oslo, NO-0317 Oslo, Norway
[i] University of Rome "La Sapienza", I-00185 Rome, Italy
[j] Tampere University of Technology, FI-33100 Tampere, Finland

ARTICLE INFO

Available online 8 January 2012

Keywords:
PET
Axial geometry
Geiger-mode Avalanche Photo Diodes (G-APD)
SiPM

ABSTRACT

The AX-PET collaboration has developed a novel concept for high resolution PET imaging to overcome some of the performance limitations of classical PET cameras, in particular the compromise between spatial resolution and sensitivity introduced by the parallax error.

The detector consists of an arrangement of long LYSO scintillating crystals axially oriented around the field of view together with arrays of wave length shifter strips orthogonal to the crystals. This matrix allows a precise 3D measurement of the photon interaction point. This is valid both for photoelectric absorption at 511 keV and for Compton scattering down to deposited energies of about 100 keV. Crystals and WLS strips are individually read out using Geiger-mode Avalanche Photo Diodes (G-APDs). The sensitivity of such a detector can be adjusted by changing the number of layers and the resolution is defined by the crystal and strip dimensions.

Two AX-PET modules were built and fully characterized in dedicated test set-ups at CERN, with point-like ^{22}Na sources. Their performance in terms of energy ($R_{energy} \approx 11.8\%$ (FWHM) at 511 keV) and spatial resolution was assessed ($\sigma_{axial} \approx 0.65$ mm), both individually and for the two modules in coincidence.

Test campaigns at ETH Zurich and at the company AAA allowed the tomographic reconstructions of more complex phantoms validating the 3D reconstruction algorithms.

The concept of the AX-PET modules will be presented together with some characterization results. We describe a count rate model which allows to optimize the planing of the tomographic scans.

1. Introduction

Positron Emission Tomography is a medical imaging method which uses the signal of two coincident 511 keV photons to reconstruct a 3D image of the radio-tracer distribution [1]. The most frequently used radio-pharmaceutical is FDG.[2] If nowadays a PET scanner is a common device in hospitals, radio and hadron therapy centers, its performance is still the subject of intense research. Improving the sensitivity and the spatial resolution remains the main goal to obtain precise images while minimizing the dose rate for the patient. Common PET systems are composed of several modules where relatively short scintillating crystals are arranged radially and read out in blocks in order to reduce the number of channels.

Longer scintillating crystals would increase the sensitivity however they worsen the spatial resolution as the depth of interaction is unknown. The axial concept avoids this dilemma between resolution and sensitivity, and allows to optimize both, independently from each other.

A fully operational AX-PET demonstrator set-up with two camera modules is available. The article describes briefly the design, the functioning and the main characterization results of

---

* Corresponding author.
E-mail address: Matthieu.Heller@cern.ch (M. Heller).

[1] Now at Laboratory for Nuclear Science, Massachusetts Institute of Technology, Cambridge 02139-4307, USA.

[2] ^{18}F labeled Fludeoxyglucose.

0168-9002/$ - see front matter © 2012 Elsevier B.V. All rights reserved.
doi:10.1016/j.nima.2011.12.114

the demonstrator. The design and construction of the demonstrator are described in a more recent article [2]. Emphasis will be put here on the results from the test campaigns done at the company AAA and ETH Zurich where we used phantoms filled with ^{18}F ($\tau_{1/2} \approx 108$ min) in aqueous solution.

Limitations in the front end electronics and data acquisition system combined with the incomplete azimuthal coverage have a negative impact on the quality of the reconstructed images. A count rate model taking into account these effects is able to predict an optimized scanning plan.

2. The axial PET concept

The main characteristic of the AX-PET concept [3] is the axial arrangement of long and individually read scintillating crystals. The crystals, stacked in several layers, are aligned parallel to the longitudinal axis of the scanner (Z-axis). The (X, Y) positions of the impinging photon is given by the address of the hit crystal. The wavelength shifting (WLS) strips placed behind and perpendicularly to the crystal layer give the third coordinate (Z).

The axial concept leads to a fully unambiguous 3D position reconstruction of the annihilation photons without parallax error. The spatial resolution and the sensitivity of the PET camera module can be tuned independently by varying respectively the crystal/strip dimensions and the number of crystal layers. The 3D photon tracking capability of our concept allows the identification of the Compton interactions in the crystal matrix (Inter Crystal Scattering). Simulations suggest that a large fraction of those scattering events can be fully recovered [4].

2.1. Module design and main components

Each AX-PET module consists of six layers of eight crystals and 26 WLS strips, hence a total of 48 scintillator crystals and 156 WLS strips. The scintillating bars are made of LYSO crystals[3] and are $3 \times 3 \times 100$ mm^3 in size. The wavelength shifting strips[4] have the dimensions $3 \times 0.9 \times 40$ mm^3. The strip thickness of 0.9 mm stands for two absorption lengths thanks to high dye concentration.

Crystals and strips are read out on one side by two different type of fast Geiger-mode Avalanche Photo Diodes (G-APD) from Hamamatsu,[5] marketed as MPPC: Multi-Pixel Photon Counters. The non-read end of the WLS strip (resp. the LYSO crystal) is coated with a reflective Aluminum film. Each MPPC is individually biased and adjusted to constant gain independent of temperature variations.

To avoid dead zones the crystal layers are staggered in the Y-coordinate by half the crystal pitch (1.75 mm). The 26 WLS strips are mounted underneath each crystal layer with an air gap in the X-coordinate of 0.2 mm. The six layers of crystals and WLS strips are optically separated to avoid the propagation of the scintillation light from one layer to next ones.

A 3D view of the module is shown in Fig. 1.

2.2. Module operation

The signal of the G-APDs is amplified by individual pre-amplifiers and processed by a dedicated VLSI-ASIC in order to obtain a precise measurement of the collected charge, proportional to the energy deposition in the crystals and to the light yield in the WLS strips. The external trigger logic is based on the sum signal of all LYSO crystals of one module. The different thresholds (50 keV (LL), 400 keV (HL) and 600 keV (HHL)) are set to select 511 keV total energy deposition contained inside the module. The standard logic $\mathrm{LL} \times \mathrm{HL} \times \overline{\mathrm{HHL}}$ is used for the coincidence. The event can be either a photoelectric effect or a Compton scattering plus photoelectric effect. The zero suppressed data is read out via a VME-PC interface into a standard desktop computer. During data taking with phantoms as described in Section 4, typical coincidence trigger rates are of the order of 100 kHz while the data acquisition (DAQ) rate is an order of magnitude lower.

The front-end electronic and data acquisition system of the AX-PET demonstrator were conceived for the validation of the concept. It made to a large extent use of available components and is by no means optimized for a real PET system.

3. Module characterization

The modules were characterized with ^{22}Na point-like sources, first independently and then in coincidence using two different dedicated set-ups. For the characterization of the AX-PET module performances, only the photoelectric absorption events are used. The detection efficiency, uniformity, energy resolution and axial resolution were determined for both module. An energy calibration was performed in order to take into account the MPPC saturation. For 511 keV photons, the deviation from linearity was around 5%.

We summarize the main performance figures and refer to Ref. [2] for further details:

- the detection efficiency is characterized by an attenuation length $\lambda_{511} = (11.9 \pm 0.1)$ mm, in very good agreement with the nominal value from LYSO data sheets;
- the average energy resolution is $(11.78 \pm 0.04)\%$ (FWHM) for single crystals and 12.8% (FWHM) for the module sum;
- the intrinsic axial resolution of the two modules is 1.75 mm and 1.82 mm (FWHM) respectively;
- the confocal axial resolution of the two modules in coincidence is 1.34 mm (FWHM), in very good agreement with the value expected from the single module resolutions;
- a time resolution of 800 ps is achieved without any optimization done in this direction.

4. Demonstrator for tomographic image reconstruction

Ideal tomographic reconstruction requires to measure lines of response under all possible angles with constant operational conditions. This means that the detector should have full 2π azimuthal coverage and be free of dead time, pile up and other rate dependent effects. Any of these effects, if uncorrected, may deteriorate the reconstructed images and lead to artifacts.

4.1. Demonstrator set-up

In order to mimic a full ring PET scanner with only two modules, a special gantry on a transportable platform was conceived. As shown in Fig. 2, it comprises a rotating phantom support and allows to rotate one module out of the face-to-face configuration. The two modules are separated by 150 mm. In the face-to-face (F2F) configuration, the size of the cylindrical field of view (FOV) is approximately $30\varnothing \times 80(z)$ mm^2. For a full scan, the phantom needs to be rotated by 180° with steps of 20°. For larger size phantoms, the FOV can be extended by rotating one of

---

[3] $\mathrm{Lu_{1.8}Y_{0.2}SiO_5}$:Ce, produced by Saint-Gobain Cristaux, 77794 Nemours, France, marketed as PreLudeTM 420.

[4] Type EJ-280-10x from Eljen Technology, Sweetwater Texas 79556, United States.

[5] Hamamatsu Photonics K.K., Japan.

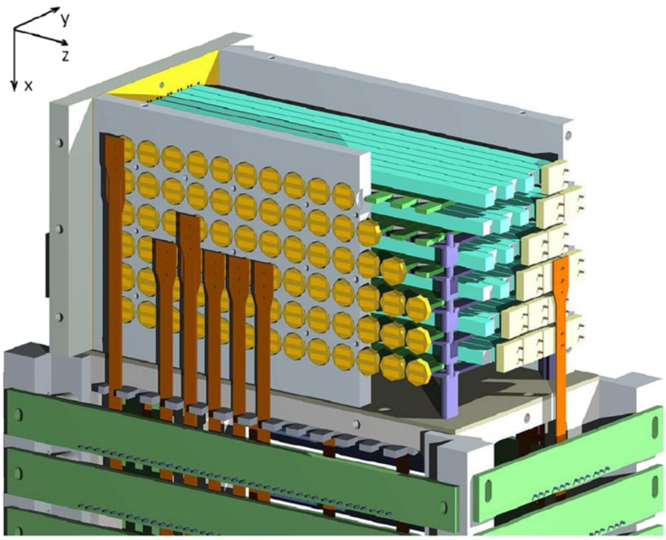

Fig. 1. Schematics of the AX-PET camera module. Some components have been removed for better clarity.

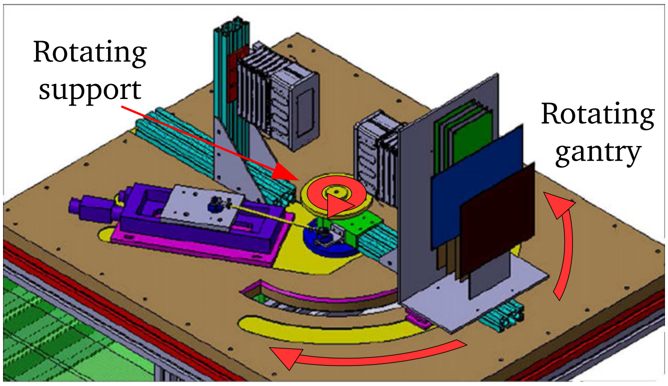

Fig. 2. 3D view of the platform where the gantry and the rotating support are mounted to ensure an extended field of view.

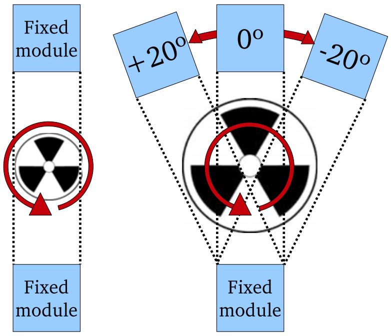

Fig. 3. The left scheme (F2F) demonstrates how the set-up is used to scan an object fully contained in the FOV whereas the right one (OBL) shows how to operate when the object size exceeds the FOV.

the two modules by ± 20° as shown in Fig. 3. In this oblique (OBL) configuration the phantom needs to perform a full rotation of 360° again in steps of 20°. In such a case, steps in F2F and 18 in OBL configuration are needed. Like this we mimic a scanner with an 18-modules ring.

In order to achieve images with reasonably low noise fluctuations, typically one million coincidence events per step are required. Given the limited data acquisition rate (~ 10 kHz) and the rapidly decaying phantom activity ($\tau_{1/2}(^{18}F) \approx 108$ min), this requirement leads to long runs (several hours) with changing experimental conditions. In Section 5 we will present a model which takes into account all relevant rate dependent effects and allows to predict a strategy for optimum data taking. Alternatively these effects can also be corrected offline.

Several measurement campaigns using phantoms filled with ^{18}F in aqueous solution were performed at ETH,[6] Zurich and the company AAA,[7] Saint Genis-Pouilly. Capillaries, a micro Derenzo, a mini Deluxe and a mouse-like phantom (NEMA NU4) were used.

Most of the runs were performed with the phantoms filled to an initial activity of 30 MBq.

4.2. *Tomographic reconstruction*

The system as described in the previous sections leads to several challenges for the tomographic reconstruction. These are for example the different nature of the transaxial (discrete) and axial (continuous) coordinates, the gaps in the geometry, and the long acquisition times. They required the development of dedicated models and reconstruction algorithms. For the time being we base the analysis on so-called golden events which correspond to a single LYSO crystal hit per module (photoelectric absorption) associated with a single WLS cluster. More complex events involving Compton scattering in the crystal matrix are the subject of ongoing studies which are expected to lead to an increased sensitivity.

Several methods are being used, either statistical or analytical. The statistical method is based on iterative maximum-likelihood expectation maximization (MLEM). Two different approaches were developed. One computes off-line a high precision system response matrix providing a very accurate modeling. However due to the complexity of the system it is very CPU time consuming and little flexible. The other computes the system response matrix on-the-fly using Siddon ray tracing and response functions [5,6]. The analytical sinogram based method provides in addition a technique to fill the sensitivity gaps between the modules [7].

An example of an image reconstructed with the statistical method (60 iterations) is shown in Fig. 4. The data was taken with a fix acquisition time per step without correcting for any rate dependent effects.

5. Optimization of the scanning procedure

The operation of our demonstrator set-up with only two modules as described in Section 4.1 compromised by the lack of azimuthal coverage and a limited data acquisition rate. As a consequence of the decaying phantom activity, we are confronted with changing operational conditions during the run. Dead time and saturation effects can mask the underlying geometrical information. Similarly pile-up of events at high activity has a strong impact on the golden event efficiency.

In the following section we develop a method that takes into account the full rate dependent system response together with the geometry of the phantom in order to predict the optimum time or the number of events needed for each step of the scan.

Theoretically the geometrical component, i.e. the combination of the phantom and the module configuration, could be computed analytically or using a Monte Carlo simulation. We have chosen a different approach by extracting the geometry from the data after

---

[6] Radio pharmaceutical Institute, ETH Zurich, CH-8093 Zurich, Switzerland.

[7] Advanced Accelerator Applications, Saint Genis-Pouilly, France.

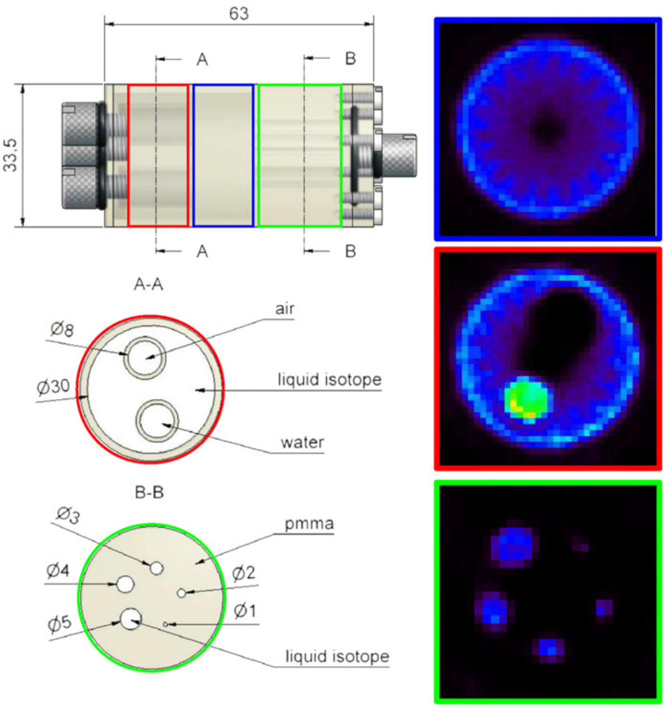

Fig. 4. 3D view of the NEMA phantom and the according reconstructed images. The different regions of interest are shown and frames with distinctive colors: blue for homogeneity, red for contrast and green for resolution capability. (For interpretation of the references to color in this figure legend, the reader is referred to the web version of this article.)

having corrected the activity dependent effects, namely the data acquisition rate and the golden event fraction. In order to do so, a short pre-scan is performed with about 1 min per step.

We present the method using the example of the NEMA phantom, however the method was successfully applied for all phantoms.

5.1. Description of the method

We first develop a model of the DAQ rate as a function of the activity. This proceeds via the understanding of the single module rate and the trigger rate (coincidence rate). All these rates are accessible via a VME scaler which is integrated into the DAQ system.

The hit rate of a single module is the product of three terms: the phantom activity (A), the detection efficiency ϵ of the module and the solid angle $d\Omega$ of the respective phantom-module configuration. The behavior is not completely linear as at high activity the system starts to be paralyzed due to pile up events. The time constant for the paralysable behavior will be denoted as τ_{P_S}. The single rate (R_S) can then be expressed as a function of the activity:

$$R_S = A \cdot d\Omega \cdot \epsilon \cdot e^{-A \cdot d\Omega \cdot \epsilon \cdot \tau_{P_S}} \qquad (1)$$

Fig. 5 shows this functional relation with the parameters $d\Omega \cdot \epsilon$ and τ_{P_S} fitted to the data taken in the F2F and OBL configurations. The parameter $\tau_{P_S} \approx 395$ ns corresponds approximately to twice the length of the sum signal. The product $d\Omega \cdot \epsilon$ is close to 0.023 sr matching the expectations from detection efficiency and geometry. As expected, for single modules there is no significant difference between the two configurations.

The trigger rate (R_T) relates linearly to the single rate with the proportionality factors being the detection efficiency of the second module ϵ and a geometrical reduction factor f_g.

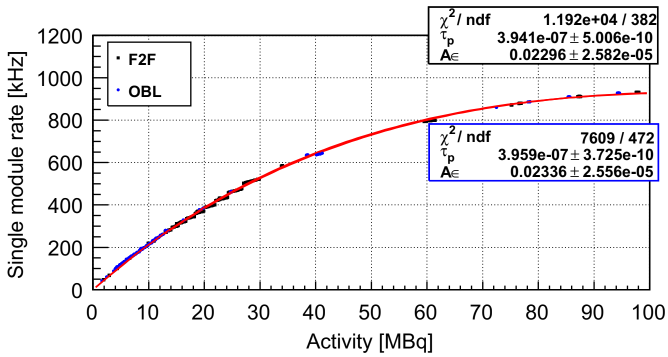

Fig. 5. Rate of a single module as function of the activity for F2F and OBL configurations. The saturation effect observed at high activity is related to pile-up.

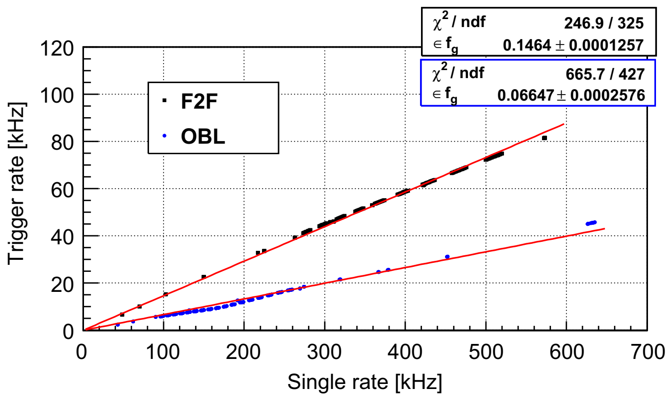

Fig. 6. Trigger rate as a function of the single rate.

The geometrical reduction factor would be one in the case of a point-like source positioned exactly in the center of the FOV for a F2F configuration, and lower than one in all other cases:

$$R_T = \epsilon \cdot f_g \cdot R_S \qquad (2)$$

Fig. 6 shows the relation between trigger and single rate. As expected, the relation is linear with a clear difference between the F2F and OBL configuration.

The DAQ rate dependence with the trigger rate requires the convolution of a paralysable and a non-paralysable component (see Eq. (3)). The non-paralysable component has a time constant (τ_{NP_D}) which corresponds to the minimum time taken by the acquisition system to process an event, even with zero length. During this time, the acquisition system is vetoed and no further event can be treated. The paralysable component reflects the increased amount of data due to pile-up at high activity which lengthens the acquisition time. It is characterized by τ_{P_D}. This leads to a saturation of the DAQ rate and at the highest activities even to a slight reduction:

$$R_D = \frac{R_T \cdot e^{-R_T \cdot \tau_{P_D}}}{1 + \tau_{NP_D} \cdot R_T \cdot e^{-R_T \cdot \tau_{P_D}}} \qquad (3)$$

Fig. 7 shows that this paralysable/non-paralysable model reproduces very well the data. The time constants found are $\tau_{NP_D} \approx 40$ μs, and $\tau_{P_D} \approx 13$ μs for F2F and 17 μs for OBL. These quantities match well the vetoed period of the DAQ system measurements directly in the F2F configuration, $\tau_{NP_D} \approx 33$ μs and $\tau_{P_D} \approx 15.6$ μs.

Convoluting equations (1)–(3) allow to derive the DAQ rate dependency with the activity separately for the configurations F2F or OBL. Fig. 8 displays the final fit which is applied to the data.

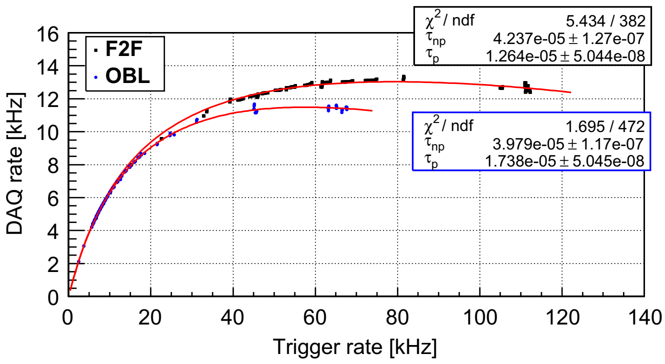

Fig. 7. DAQ rate as a function of the trigger rate.

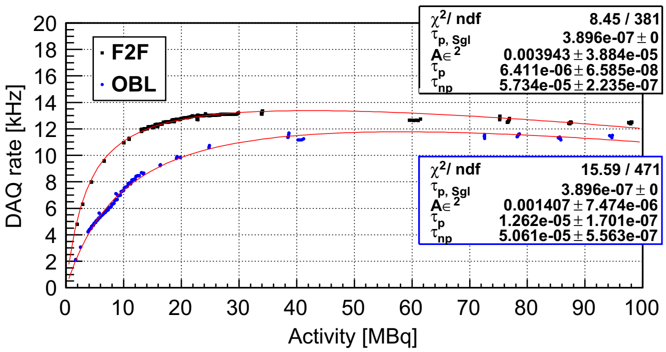

Fig. 8. DAQ rate as a function of the activity. The difference between the F2F and OBL configuration is related to the solid angle of the modules in coincidence.

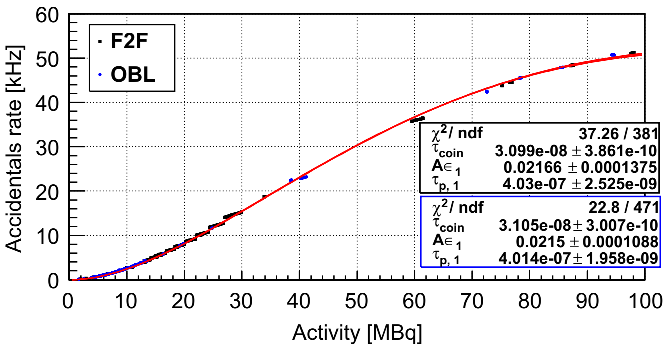

Fig. 9. Accidental rate as a function of the phantom activity.

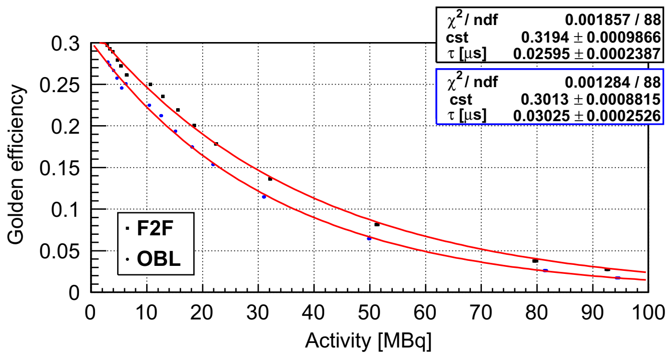

Fig. 10. Efficiency of the golden events as a function of the activity. At high activity the efficiency drops due to the pile-up.

The data appear to be properly modeled over the complete activity range up to 100 MBq.

A further quantity of interest is the rate of accidental coincidences (R_A). With the set-up, the accidental rate is measured with the delayed coincidence technique, delaying the signal from one module by at least 200 ns. The measurement is fitted using the theoretical formula for the accidental rate:

$$R_A = 2 \cdot \tau_{coinc} \cdot R_S^2 \tag{4}$$

where τ_{coinc} is the length of the coincidence window. As shown in Fig. 9 the fitted coincidence window of ~ 31 ns matches well the set value of 30 ns. As the accidental rate is driven by the single module rates, no difference for F2F and OBL configurations is expected (see Fig. 5).

Finally the fraction of the golden events, which are the basis for the tomographic reconstruction, is affected by pile-up effects and therefore dependent on the activity and geometrical configuration. This quantity needs to be extracted from the data in an offline analysis. As shown in Fig. 10 the golden event fraction is well described by an exponential dependence on the activity. The ratio of accidentals to true coincidences is less favorable for the OBL configuration which explains its lower golden event fraction.

With the above model, the pre-scan data allows to separate off the geometrical component for each of the 27 steps.

Based on an initial phantom activity of the real scan, the model allows to predict the golden event rate at a given time for any geometrical configuration (i.e. scan step). In order to account for the decay of the source activity, the calculations are performed in time intervals of 1 s. While preserving the geometrical component of the 27 steps, an overall normalization is applied to ensure that for none of the steps less than one million golden events are recorded.

5.2. *Results*

To validate the model we compare the number of measured golden events with the model based prediction. Fig. 11 presents as an example the results for the NEMA phantom. The relative difference is typically ±2% and for none of the 27 steps exceeds 4%. Fig. 12 compares the measured and predicted golden event fraction along the entire scan. The deviation at the end of the scan sequence is still below 1%.

The model appears to provide a realistic and precise description of the golden event rate along a full measurement scan which can last several hours. For our demonstrator based on two detector modules, it allows to optimize the scan sequence for maximum statistics in a given time. In addition the data does not need further corrections before being reconstructed. Data taken following this scheme has been reconstructed and recently published [8].

6. Summary and outlook

The results presented in this article validate the AX-PET concept and its ability to reconstruct tomographic images with high resolution. The particularity and flexibility of its design allow to tune independently spatial resolution and sensitivity and make it suitable for a range of PET applications, from small animal to full body PET.

The operation of the AX-PET demonstrator set-up, which consists only of two detector modules, is compromised by the incomplete ring coverage and limitations in the front-end and acquisition system. The presented count rate model takes into account the relevant geometrical and rate dependent effects and

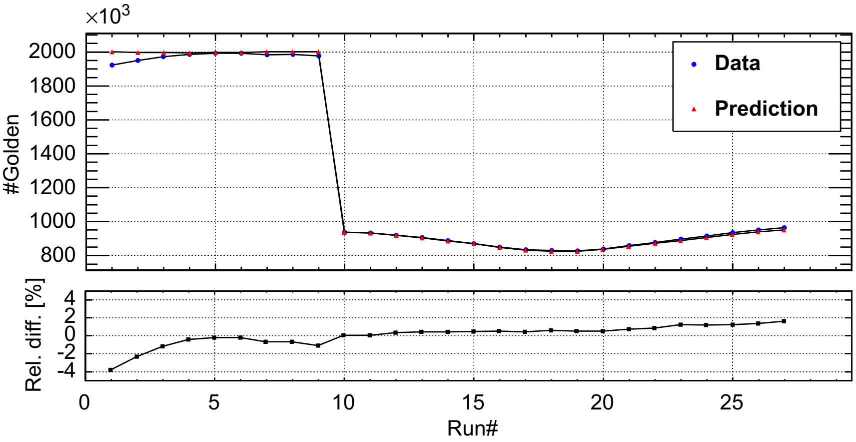

Fig. 11. The upper graph presents the absolute number of golden events for the prediction and the data. The bottom curve shows the relative difference between the two.

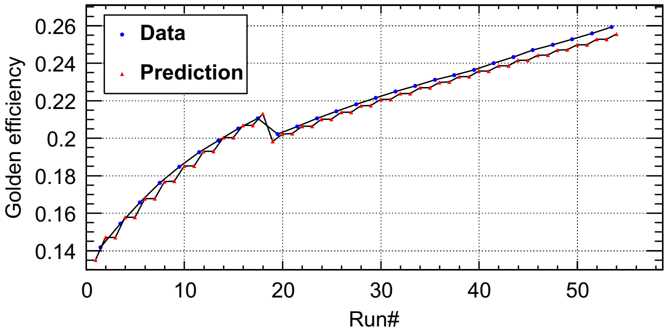

Fig. 12. Comparison of the golden efficiency predicted and the one extracted from the data along the different steps of a scan.

permits the prediction of an optimized scanning plan which maximizes the data sample for the tomographic reconstruction. The model was successfully applied during a test campaign in July 2011 and led to high quality images [8].

The AX-PET demonstrator is described by a comprehensive Gate/Geant4 model which was validated by measured data [9]. The model will now be used to study the performance of dedicated full ring geometries, optimized e.g. for brain imaging.

Acknowledgments

We would like to thank our technical staff for their competent and efficient support. The work is partially funded through the Spanish Ministry of Science & Innovation under Grant FPA2010-14891. Paola Solevi is supported by the Marie Curie Intra-European Fellowship Grant 237620 for the project INSPET (European Commission). Matthieu Heller is supported through the MarieCurie Initial Training Network MC-PAD (Grant no.214560-2).

References

[1] H. Zaidi, Zeitschrift für Medizinische Physik 16 (2006).
[2] P. Beltrame, et al., Nuclear Instrumentation and Methods in Physics Research Section A 654 (2011) 546.
[3] 〈https://cern.ch/twiki/bin/view/AXIALPET〉.
[4] M. Rafecas, et al., Physics in Medicine and Biology 48 (7) (2003) 821.
[5] J. Gillam, P. Solevi, J.F. Oliver, M. Rafecas, in: Fully 3D 2011 Conference Proceedings, Potsdam, Germany.
[6] J. Gillam, P. Solevi, J.F. Oliver, M. Rafecas, in: IEEE NSS-MIC 2011 Proceedings, Valencia, Spain, submitted for publication.
[7] U. Tuna, et al., in: Proceedings at IEEE NSS MIC 2011 conference on Analytical Image Reconstruction Strategies for AX-PET Data, submitted for publication.
[8] M. Rafecas, et al., in: Proceedings at IEEE NSS MIC 2011 Conference on The AX-PET Concept: New Developments And Tomographic Imaging, submitted for publication.
[9] P. Solevi, et al., Description and Validation of a full model of AX-PET Based on GEANT4 and GATE, in: Proceedings of the SPIE 2011 Medical Imaging Conference.